Vol. 35 • No. 9 • February 26 • 2025

www.afm-journal.de

ADVANCED FUNCTIONAL MATERIALS

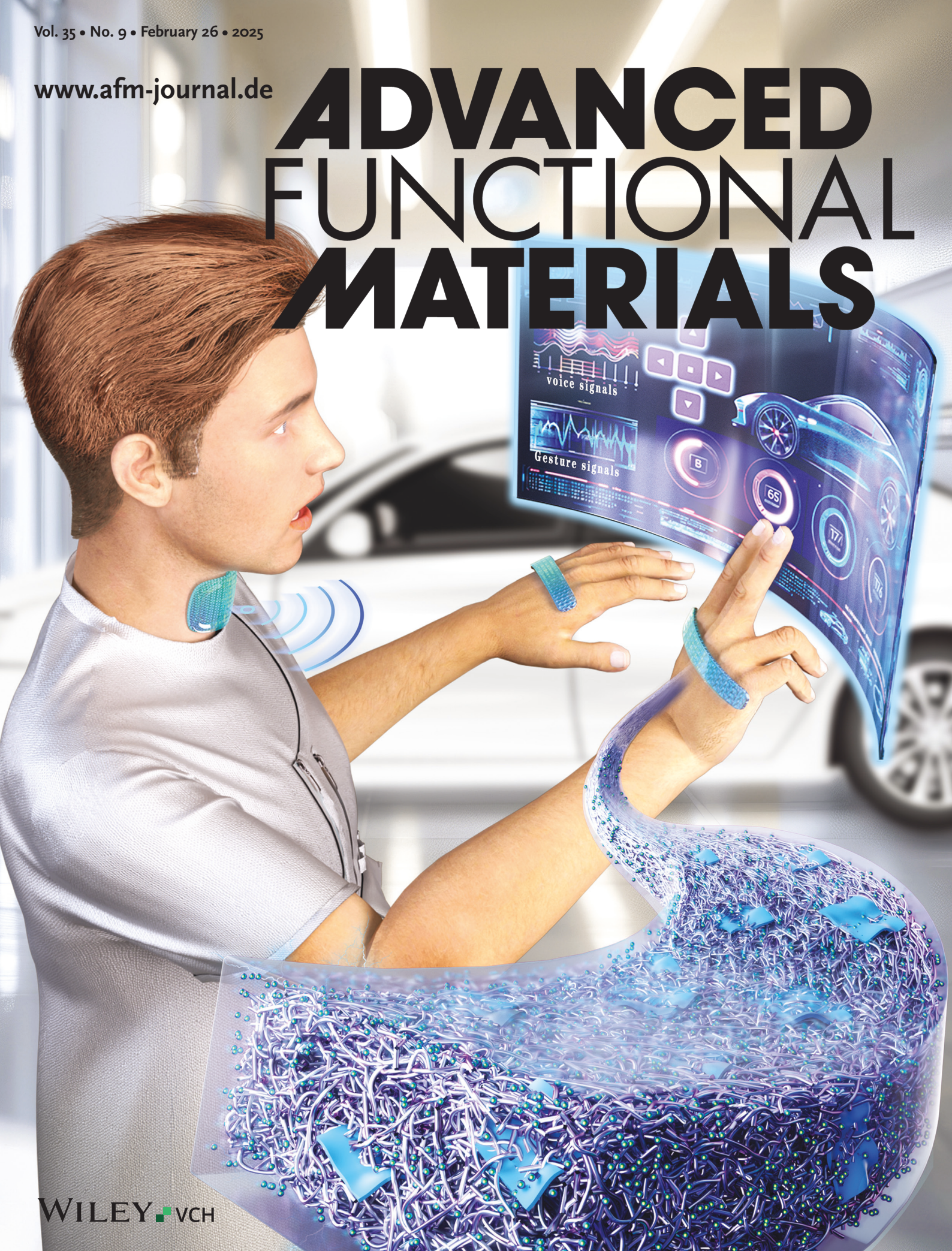

WILEY VCH

ADVANCED FUNCTIONAL MATERIALS
www.afm-journal.de

Multi-Functional $Ti_3C_2T_x$-Silver@Silk Nanofiber Composites With Multi-Dimensional Heterogeneous Structure for Versatile Wearable Electronics

Nuozhou Yi, Cheng Zhang, Zhen Wang, Zhonghua Zheng, Jiahao Zhou, Ruzhi Shang, Peidi Zhou, Chan Zheng, Minghua You, Huamin Chen,* Huanyu Cheng,* and Mingcen Weng**

Silk nanofibers (SNFs) from abundant sources are low-cost and environmentally friendly. Combined with other functional materials, SNFs can help create bioelectronics with excellent biocompatibility without environmental concerns. However, it is still challenging to construct an SNF-based composite with high conductivity, flexibility, and mechanical strength for all SNF-based electronics. Herein, this work reports the design and fabrication of Ti_3C_2Tx-silver@silk nanofibers (Ti3C2Tx-Ag@SNF) composites with multi-dimensional heterogeneous conductive networks using combined in situ growth and vacuum filtration methods. The ultrahigh electrical conductivity of $Ti_3C_2T_x$-Ag@SNF composites (142959 S m^{-1}) provides the kirigami-patterned soft heaters with a rapid heating rate of 87 °C s^{-1}. The multi-dimensional heterogeneous network further allows the creation of electromagnetic interference shielding devices with an exceptionally high specific shielding effectiveness of 10,088 dB cm^{-1}. Besides working as a triboelectric layer to harvest the mechanical energy and recognize the hand gesture, the $Ti_3C_2T_x$-Ag@SNF composites can also be combined with an ionic layer to result in a capacitive pressure sensor with a high sensitivity of 410 kPa^{-1} in a large range due to electronic-double layer effect. The applications of the $Ti_3C_2T_x$-Ag@SNF composites in recognizing human gestures and human-machine interfaces to wirelessly control a trolley demonstrate the future development of all SNF-based electronics.

1. Introduction

Huge application potential in personal intelligent medical systems, human-machine interfaces, human physiological signal monitoring, and intelligent robots has spurred the rapid development of wearable electronics.[1–8] However, the commonly used flexible and stretchable substrates are not breathable and do not provide high strength, posing critical challenges in long-term use.[9] As the main component in traditional wearable products, natural silk is associated with the advantages of softness, breathability, and malleability.[10] Compared with other nanofiber materials made from nature (e.g., chitin nanofibers, cellulose nanofibers, bacterial cellulose, and nanocrystalline cellulose),[11–14] the silk nanofibers (SNFs) are low-cost and easy to prepare from a safe and non-toxic preparation process (Tables S1, S2, Supporting Information). However, the lack of electrical conductivity limits their application in wearable electronics. Efforts to address this issue have led to the creation of

N. Yi, Z. Wang, J. Zhou, C. Zheng, M. You, M. Weng
School of Materials Science and Engineering
Fujian University of Technology
Fuzhou, Fujian 350118, China
E-mail: czheng@fjut.edu.cn; wengmc@fjut.edu.cn
N. Yi, Z. Wang, C. Zheng, M. You, M. Weng
Institute of Biology and Chemistry
Fujian University of Technology
Fuzhou 350118, China
The ORCID identification number(s) for the author(s) of this article can be found under https://doi.org/10.1002/adfm.202412307

DOI: 10.1002/adfm.202412307

C. Zhang, R. Shang, H. Chen
Fujian Key Laboratory of Functional Marine Sensing Materials
College of Materials and Chemical Engineering
Minjiang University
Fuzhou 350108, China
E-mail: chenhuamin@mju.edu.cn
Z. Zheng
Concord University College
Fujian Normal University
Fuzhou 350117, China
R. Shang
College of Mechanical and Electrical Engineering
Fujian Agriculture and Forestry University
Fuzhou 350108, China
P. Zhou
School of Smart Marine Science and Technology
Fujian University of Technology
Fuzhou, Fujian 350118, China

silk-based conductive composites by combining silk with conductive organic/inorganic functional materials such as carbon-based materials, metal-based nanomaterials, and conductive polymers through surface modification, fine control of the interfacial assembly process, and post-processing strategies.[15–18] However, the silk-based conductive composites prepared by physical methods (e.g., immersion, stirring, vacuum filtration, etc.) exhibit poor interfacial adhesion and low conductivity due to low loading of conductive materials.[19–24] Dissolving silk into a silk fibroin solution and combining it with conductive materials for spinning can be another solution to create silk-based conductive composite fibers,[16] but the regenerated silk fibers often show poor flexibility and strength. Although converting silk into nitrogen-doped carbonaceous materials opens a new door,[25–27] carbonized silk materials do not yet have the original flexibility and mechanical strength of natural silk. Therefore, it is still of high interest to create silk-based composites with excellent electrical conductivity, flexibility, and mechanical strength.

MXene, as a two-dimensional transition metal carbide, has excellent conductivity, thermal conductivity, and electronegativity, having broad prospects in fields such as electrothermal heaters, flexible sensors, electromagnetic interference (EMI) shielding devices, and triboelectric nanogenerators (TENGs).[28–31] Shen et al. used silk fibers (SF) as a bridging agent to assemble SF@MXene composite film with a continuous corrugated layered macroscopic structure. The pressure sensor based on the SF@MXene composite film has a low detection limit of 9.8 Pa and a sensitivity of 25.5 kPa^{-1}.[32] Also, Zhang et al. used vacuum spraying technology to combine silver nanowires and $Ti_3C_2T_x$ nanosheets onto conductive silk textiles, which were applied in EMI shielding and humidity sensors.[33] Natural 1D materials such as silk are commonly used as mechanical performance enhancing fillers to enhance the mechanical properties of wearable devices. However, due to the non-conductivity of natural silk, the conductive substrate inevitably experiences a decrease in conductivity after doping with natural fiber materials. One solution is to introduce conductive metals, such as metallic silver.[34] Silver has a high conductivity and can effectively reduce interfacial resistance. For example, Xie et al. proposed a silver nanoparticles (AgNPs)@MXene heterogeneous structure decorated graphite composite film achieved low voltage driven Joule heating response (reaching 128 °C at 2.7 V in 100 s) and excellent electromagnetic shielding efficiency (58 dB).[35] However, excessive self-stacking of $Ti_3C_2T_x$ MXene can lead to stress concentration, brittle fracture, and decrease the mechanical properties of the composite material, which cannot meet the requirements of wearable devices.

Here, we report the design and fabrication of $Ti_3C_2T_x$-silver@silk nanofiber ($Ti_3C_2T_x$-Ag@SNF) composites with multi-dimensional heterogeneous network structures through combined physical (vacuum filtration) and chemical (in situ growth) methods. Specifically, after in situ growth of zero-dimensional (0D) AgNPs on the surface of one-dimensional (1D) SNFs by using the silver mirror reaction to construct Ag@SNF composites, introducing 2D $Ti_3C_2T_x$ nanosheets as reinforcement fillers yields $Ti_3C_2T_x$-Ag@SNF composites with high conductivity and mechanical strength. The high conductivity and multi-dimensional heterogeneous network structures of $Ti_3C_2T_x$-Ag@SNF composites are showcased in the proof-of-the-concept demonstrations in personal thermal management, EMI shielding devices, TENGs, pressure sensors, and human-machine interfaces. Incorporating multifunctionality, portability, and flexibility, $Ti_3C_2T_x$-Ag@SNF composites have broad application prospects in the field of wearable electronic devices.

2. Results and Discussion

2.1. Design, Fabrication, and Characterization of Ti_3C_2Tx-Ag@SNF Composites

The fabrication of $Ti_3C_2T_x$-Ag@SNF composites starts with the preparation of multilayer $Ti_3C_2T_x$ (**Figure 1a**) by etching the MAX phase Ti_3AlC_2 powder by in situ HF generation of HCl/LiF, followed by intercalation with dimethyl sulfoxide (DMSO) to obtain the two-dimensional (2D) $Ti_3C_2T_x$ nanosheets aqueous dispersion (Figure S1, Supporting Information). Next, the degummed silk from liquid-phase stripping by using a calcium chloride/ethanol/water mixed solution yields the SNFs dispersion (Figure S2a, Supporting Information). Thanks to the hierarchical structure of natural silk, the surface of SNFs has abundant oxygen-containing functional groups with negative zeta potential (Figure S2b, Supporting Information), which can help SNFs to adsorb positive Ag^+ in silver ammonia solution by electrostatic action to form AgNPs. As a result, in situ growing of zero-dimensional (0D) AgNPs on the surface of 1D SNFs using silver ammonia solution in a lightless environment gives Ag@SNF composites aqueous dispersions (Figure 1b). With added glucose solution as a reducing agent, less free energy is required to nucleate Ag^+ on the surface of SNFs, according to the heterogeneous nucleation mechanism.[34] As a result, the Ag^+ immobilized on the surface of SNFs is nucleated first, which decreases the concentration of Ag^+ on the surface of SNFs (the solid-liquid interface). Breaking the complexing equilibrium of $[Ag(NH_3)_2]^+$ and Ag^+ further dissociates $[Ag(NH_3)_2]^+$ to Ag^+. The gradual growth of the silver nuclei into AgNPs on the surface of the SNFs covers the surface of the SNFs and forms Ag@SNF composites with a yellow color (Figure S3, Supporting Information). The microstructure and element characterizations of Ag@SNF composites with TEM and EDS confirm the formation of AgNPs on SNFs (Figures S3, S4, Supporting Information). Finally, vacuum filtration of the $Ti_3C_2T_x$ nanosheet and Ag@SNF composites yields the flexible dark greenish $Ti_3C_2T_x$-Ag@SNF composites film with hierarchical structure (0D AgNPs uniformly attached on the surface of 1D SNFs and coated with 2D $Ti_3C_2T_x$ nanosheets) (Figure 1c–e; Figure S5, Supporting Information). The rich oxygen-containing functional groups on the surface of Ag@SNF composites form hydrogen bonding with $Ti_3C_2T_x$ nanosheets with tight attachment. The $Ti_3C_2T_x$-Ag@SNF composites with hierarchical structures, high electrical conductivity, and flexibility provide broad application

H. Cheng
Department of Engineering Science and Mechanics
The Pennsylvania State University
University Park 16802, USA
E-mail: huanyu.cheng@psu.edu

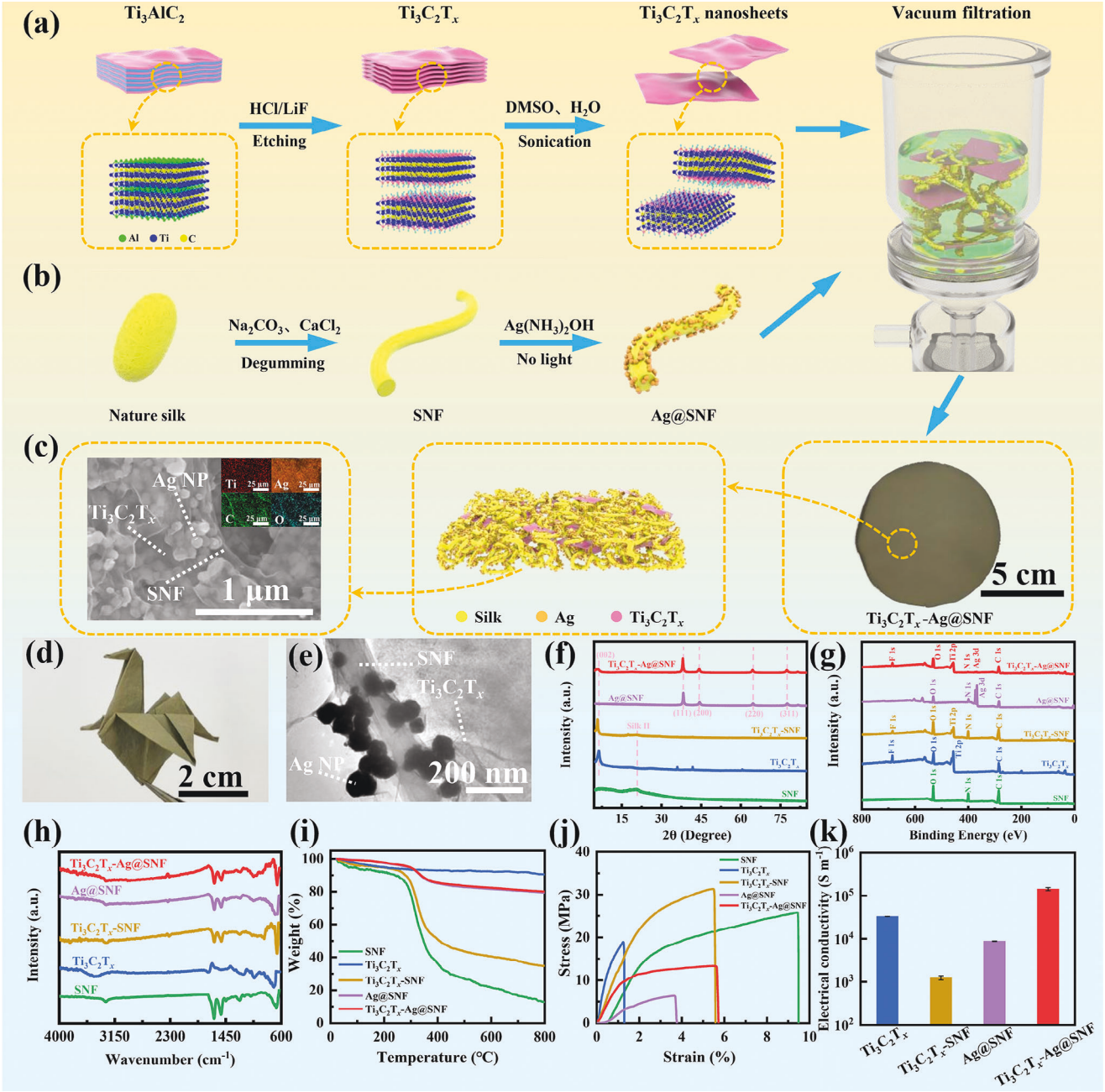

Figure 1. Fabrication and characterizations of $Ti_3C_2T_x$-Ag@SNF Composites. Schematic showing the fabrication process of a) $Ti_3C_2T_x$ nanosheets and b) Ag@SNF composites. c) SEM, schematic, and optical images of the $Ti_3C_2T_x$-Ag@SNF composite. d) Origami of $Ti_3C_2T_x$-Ag@SNF composite film showing its flexibility. e) TEM image of $Ti_3C_2T_x$-Ag@SNF composites. f) XRD patterns, g) XPS spectra, h) FTIR spectra, i) TG curves, j) strain–stress curves, and k) electrical conductivity of SNF, $Ti_3C_2T_x$, $Ti_3C_2T_x$-SNF composites, Ag@SNF composites, and $Ti_3C_2T_x$-Ag@SNF composites (sample size = 5).

opportunities in personal thermal management, electromagnetic interference shielding, triboelectric nanogenerators (TENG), and pressure sensors.

The material composition and content of $Ti_3C_2T_x$-Ag@SNF composites are further characterized with X-ray diffractometer (XRD), X-ray photoelectron spectroscopy (XPS), Fourier transform infrared spectrometer (FTIR), and thermogravimetry (TG) analysis. The phase structures of $Ti_3C_2T_x$-Ag@SNF composites and their precursors analyzed by XRD reveal a strong diffraction peak at 20° for the SNFs caused by the silk II structure.[36] Four main diffraction peaks at 38.3/44.4/64.6/77.6° in Ag@SNF composites correspond to the (111)/(200)/(220)/(311) crystal planes of Ag,[37] indicating successful loading of AgNPs on SNFs. The near disappearance of diffraction peaks of SNFs after the silver plating indicates the major coverage of generated AgNPs by the silver mirror reaction over the surface of SNFs. Diffraction

peaks at 7°/20° for $Ti_3C_2T_x$/$Ti_3C_2T_x$-SNF composites from the (002) crystal plane of $Ti_3C_2T_x$ and the silk II structure of SNF[38] (Figure 1f), indicating $Ti_3C_2T_x$ nanosheets on SNFs. The simultaneous appearance of diffraction peaks of the silk II structure from SNFs, the (002) crystal plane from $Ti_3C_2T_x$, and the four crystal planes from AgNPs on the XRD pattern of $Ti_3C_2T_x$-Ag@SNF composites indicates successful loading of $Ti_3C_2T_x$ nanosheets and AgNPs onto SNFs. The surface chemical compositions analyzed by XPS[39–41] show new Ti 2p, F 1s, and Ag 3d characteristic peaks from $Ti_3C_2T_x$-SNF composites and Ag@SNF in addition to the three characteristic peaks of O 1s, N 1s, and C 1s from SNFs, confirming successful attachment of $Ti_3C_2T_x$ nanosheets and AgNPs on SNFs (Figure 1g). In comparison, no new peaks in the XPS spectrum of $Ti_3C_2T_x$-Ag@SNF composites indicate physical adsorption and entanglement of $Ti_3C_2T_x$ and Ag-SNF composites without further forming new chemical bonds (Figures S6–S10, Supporting Information). Furthermore, the FTIR spectra of SNFs and Ag@SNF composites show almost the same surface functional groups to indicate no significant effect of AgNPs on SNFs (Figure 1h). The absorption band around 1520 cm^{-1} is caused by the C-N telescopic vibration in amide II and the bending vibration of N-H.[42] The absorption band of $Ti_3C_2T_x$ around 700 cm^{-1} is related to the vibration of Ti-O.[43] In addition to typical absorption bands of $Ti_3C_2T_x$ and SNFs, the $Ti_3C_2T_x$-SNF and $Ti_3C_2T_x$-Ag@SNF composites also show a shift in the absorption band from 1520 to 1510 cm^{-1}, indicating a strong hydrogen bonding between $Ti_3C_2T_x$ and SNFs.[44]

The thermal stability analysis with TG reveals a small amount of weight loss in all samples containing SNFs at the low temperature (25–200 °C), which results from the water evaporation from the above samples. The more significant weight loss occurs in the temperature range from 300 to 400 °C due to the decomposition of SNFs at high temperatures (Figure 1i). The remaining mass of 80% from $Ti_3C_2T_x$-Ag@SNF is close to 79% and 90.6% from Ag@SNF and $Ti_3C_2T_x$, but significantly higher than 12.8% and 34.8% from SNF and $Ti_3C_2T_x$-SNF. The TG curve of $Ti_3C_2T_x$-Ag@SNF composites is almost unchanged even above 400 °C, indicating excellent thermal stability. Assuming no loss of the AgNPs during the fabrication process, the mass fractions of SNF, $Ti_3C_2T_x$, and AgNPs in $Ti_3C_2T_x$-Ag@SNF composites are 25.7%, 5%, and 69.3%, respectively. The consistent degradation peak positions of the samples with SNFs in the DTA curve indicate the same degradation temperature of the SNFs and little effect of the silver mirror reaction on the thermal stability of SNFs (Figure S11, Supporting Information). Relying on the interaction (physical entanglements and hydrogen bonds) between SNFs, the SNF film exhibits a fracture strain of 16.3% and fracture toughness of 1.5 MJ m^{-3} (Figure 1j; Figure S12, Supporting Information). Compared with the SNF film, the Ag@SNF composites show reduced mechanical properties across the board (e.g., fracture strain, fracture toughness, Young's modulus, etc.) due to weakened interaction between SNFs with covered AgNPs, making them prone to slip upon stretching. In contrast, $Ti_3C_2T_x$ nanosheets roughen the surface of SNFs to increase the physical friction between the SNFs for enhanced mechanical properties of $Ti_3C_2T_x$-SNF composites. Adding a small amount of $Ti_3C_2T_x$ nanosheets (m[$Ti_3C_2T_x$]: m[SNFs] = 1:4) with a high Young's modulus of 3.4 GPa increases the fracture strain, fracture stress, and fracture toughness from 3.7%, 6.9 MPa, and 0.2 MJ m^{-3} for Ag@SNF to 5.7%, 13.3 MPa, and 0.5 MJ m^{-3} for $Ti_3C_2T_x$-Ag@SNF. The enhanced mechanical properties of $Ti_3C_2T_x$-Ag@SNF composites result from the increased interaction between $Ti_3C_2T_x$ nanosheets and Ag@SNFs. The combination of insulating SNFs with conductive $Ti_3C_2T_x$ nanosheets (24692 S m^{-1}) and/or AgNPs increases the electrical conductivity of $Ti_3C_2T_x$-SNF composites (m[$Ti_3C_2T_x$]: m[SNFs] = 1:4) and Ag@SNF composites (m[$AgNO_3$]:m[SNFs] = 5:1) to 1234 S m^{-1} and 8807 S m^{-1} (Figure 1k; Figure S13, Supporting Information). Introducing a small amount of $Ti_3C_2T_x$ nanosheets (25% of the mass of SNFs) into Ag@SNF composites further increases the conductivity of $Ti_3C_2T_x$-Ag@SNF composites to 142959 S m^{-1} (0.586 Ω sq^{-1}), which is larger than most of $Ti_3C_2T_x$-based conductive films (Figure S14 and Table S3, Supporting Information). However, the low content of $Ti_3C_2T_x$ nanosheets disrupts the connection between the Ag@SNF composites to give decreased conductivity, while excessive $Ti_3C_2T_x$ nanosheet accumulation from the high content reduces the mechanical properties of $Ti_3C_2T_x$-Ag@SNF composites due to brittle fracture caused by stress concentration (Figures S15, S16, Supporting Information).[45]

2.2. Thermal Performances and Applications of Ti_3C_2Tx-Ag@SNF Composites

The $Ti_3C_2T_x$-Ag@SNF composites with multi-dimensional heterogeneous conductive networks and ultra-high conductivity can provide effective Joule heating upon applied voltage due to electrothermal conversion. For a voltage from 1 to 4 V applied on $Ti_3C_2T_x$-Ag@SNF (2 cm × 3 cm), the temperature rapidly rises to reach a steady state in 20 s (**Figure 2a**). The steady-state temperature of 159.8 °C can be obtained within 4 s with a maximum heating rate of 87 °C s^{-1} at 4 V (Figure 2b), which outperforms most $Ti_3C_2T_x$-based heaters (Table S4, Supporting Information). The linear relationship between the steady-state temperature and the square of the driven voltage follows Joule's law (Figure 2c). The electrothermal conversion efficiency of 90% (Note S1, Supporting Information) indicates excellent electrothermal performance of $Ti_3C_2T_x$-Ag@SNF composites. Removal of the driven voltage allows efficient cooling of $Ti_3C_2T_x$-Ag@SNF to room temperature within 30 s. The control in the driven voltage rapidly changes the temperature of $Ti_3C_2T_x$-Ag@SNF composites (Figure 2d). Applying a square-wave voltage results in square-wave patterns in the temperature-time curves of $Ti_3C_2T_x$-Ag@SNF composites (Figure 2e), demonstrating the controllability of $Ti_3C_2T_x$-Ag@SNF composites. The temperature of $Ti_3C_2T_x$-Ag@SNF composites can be maintained stably over 3600 s when operated at 4 V (Figure 2f).

Designed into a simple kirigami pattern, the $Ti_3C_2T_x$-Ag@SNF composites-based stretchable heater exhibits stable and uniform temperature distribution in the entire heating area (i.e., ca. 44 °C at 2.5 V upon stretching up to 250%) (**Figure 3a**), which is attributed to the negligibly small resistance change over strains and cycles (of less than 4%) (Figure 3b,c). Because of the stable performance over bending and twisting (Figure 3d), the kirigami-patterned $Ti_3C_2T_x$-Ag@SNF composites-based heaters in the band type can wrap around curvilinear surfaces such as the glass beaker and the wrist and arm (Figure 3e,f). The kirigami-patterned $Ti_3C_2T_x$-Ag@SNF composites can also serve

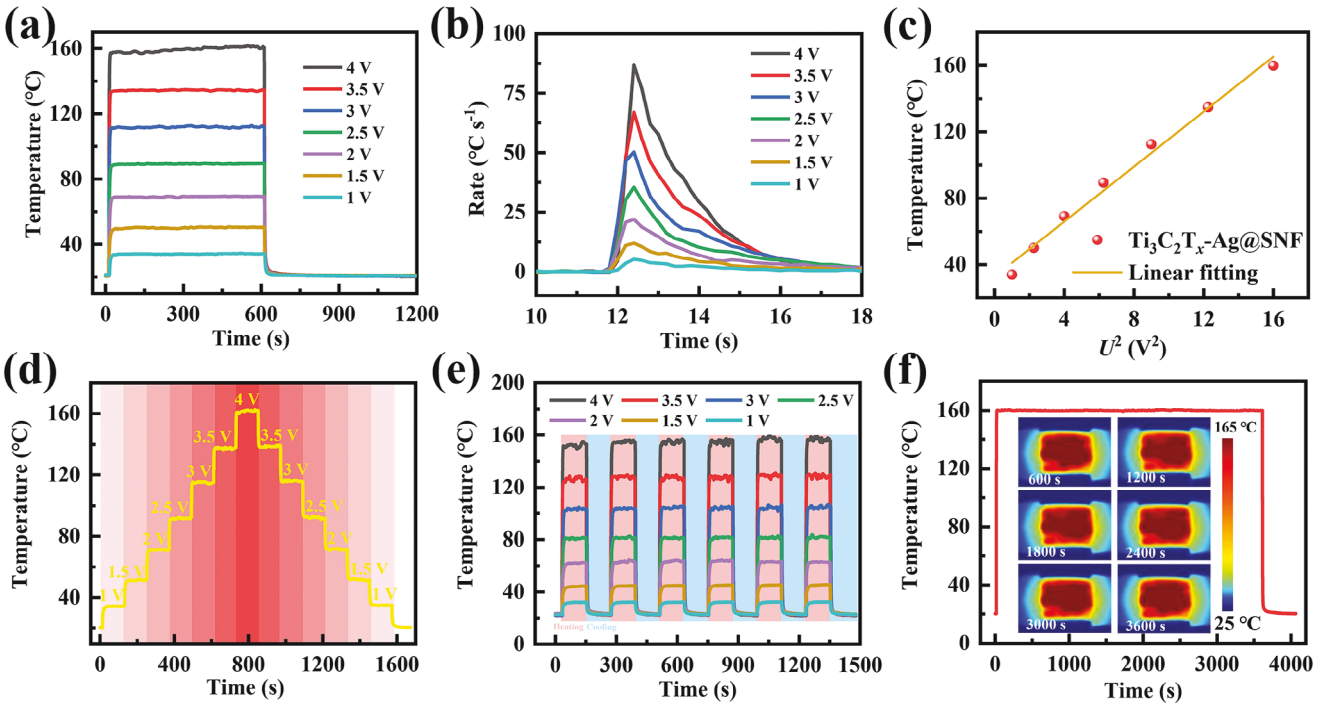

Figure 2. Thermal characterizations and applications of $Ti_3C_2T_x$-Ag@SNF composites. a) Temperature-time curves and b) heating rates of $Ti_3C_2T_x$-Ag@SNF composites at different voltages. c) Linear fit of the steady-state temperature of $Ti_3C_2T_x$-Ag@SNF composites versus U^2. d) Surface temperatures of $Ti_3C_2T_x$-Ag@SNF composites under varying voltages. e) Temperature rise and fall of $Ti_3C_2T_x$-Ag@SNF composites under different voltages. f) Joule heating performance and infrared thermal images during long-term heating of $Ti_3C_2T_x$-Ag@SNF composites at 4 V.

as a stretchable connection to provide stable light intensity in the series connected light-emitting diodes (LEDs) even upon stretching of 250% (Figure S17, Supporting Information).

2.3. EMI Shielding Performances and Applications of $Ti_3C_2T_x$-Ag@SNF Composites

The multi-dimensional conductive network of the $Ti_3C_2T_x$-Ag@SNF composite also makes it a promising candidate for EMI shielding. To evaluate EMI shielding effectiveness (SE) according to the Schelkunoffs theory, EMI SE_T values of SNF, $Ti_3C_2T_x$, $Ti_3C_2T_x$-SNF composites, Ag@SNF composites, and $Ti_3C_2T_x$-Ag@SNF composites are collected in X-band (8.4-12.4 GHz) (**Figure 4a**). Compared to the negligible EMI shielding of SNF (with the EMI SE_T of close to 0 in the X-band), the $Ti_3C_2T_x$-SNF composite exhibits increased EMI SE_T of 15.6 dB due to added conductive 2D $Ti_3C_2T_x$ nanosheets (EMI SE_T of 32.7 dB) to SNF networks. The high EMI SE_T of 28.1 dB in the Ag@SNF composites indicates that a 3D conductive network can also greatly enhance the EMI shielding ability of SNF-based composites. Combining 2D $Ti_3C_2T_x$ nanosheets with the 3D in situ polymerized AgNPs in the $Ti_3C_2T_x$-Ag@SNF composite with multi-dimensional heterogeneous network structure results in significantly increased EMI SE_T to 49.4 dB (10,088 dB cm^{-1}), outperforming the other $Ti_3C_2T_x$-based thin films (Table S5, Supporting Information). Considering the requirements of 20 dB in the commercial EMI shielding materials to shield 99% of the incident electromagnetic wave energy,[46] $Ti_3C_2T_x$-Ag@SNF composites are more than sufficient for broad applications in electromagnetic shielding.

The calculation of the contributions of EMI SE_R and SE_A to EMI SE_T reveals the EMI shielding mechanism of the $Ti_3C_2T_x$-Ag@SNF composites (Note S2, Supporting Information) (Figure 4b). Compared with the SNF film, $Ti_3C_2T_x$, $Ti_3C_2T_x$-SNF composites, Ag@SNF composites, and $Ti_3C_2T_x$-Ag@SNF composites all exhibit higher SE_T. The observation of higher SE_A than SE_R does not directly indicate absorption-dominant EMI shielding,[47] because of the attenuation of absorption of electromagnetic waves incident into the material. The determination of the EMI shielding mechanism would rely on the analysis of the power coefficient of the reflection (R), absorption (A), and transmission (T)[48] of SNF, $Ti_3C_2T_x$, $Ti_3C_2T_x$-SNF, Ag@SNF, and $Ti_3C_2T_x$-Ag@SNF composites (Figure 4c). The observation of the much higher R values than the A values for $Ti_3C_2T_x$, $Ti_3C_2T_x$-SNF, Ag@SNF, and $Ti_3C_2T_x$-Ag@SNF indicates the dominant role of the reflective shield over the absorption shield. In particular, the R value of 0.98999 is significantly higher than the A value of 0.01 and the T value of 0.00001 for $Ti_3C_2T_x$-Ag@SNF (ca. 99% of the total power of the incident electromagnetic wave is reflected). While the SE_A of 29.5 dB for $Ti_3C_2T_x$-Ag@SNF indicates that 59.7% of the electromagnetic wave incident into the $Ti_3C_2T_x$-Ag@SNF is absorbed, it is only 1% of the total electromagnetic wave power. The dominant reflection of electromagnetic waves in the EMI shielding of $Ti_3C_2T_x$-Ag@SNF composites results from the multi-dimensional conductive network (Figure 4d). The impedance mismatch at the $Ti_3C_2T_x$-Ag@SNF composite and air interface first allows the reflection of

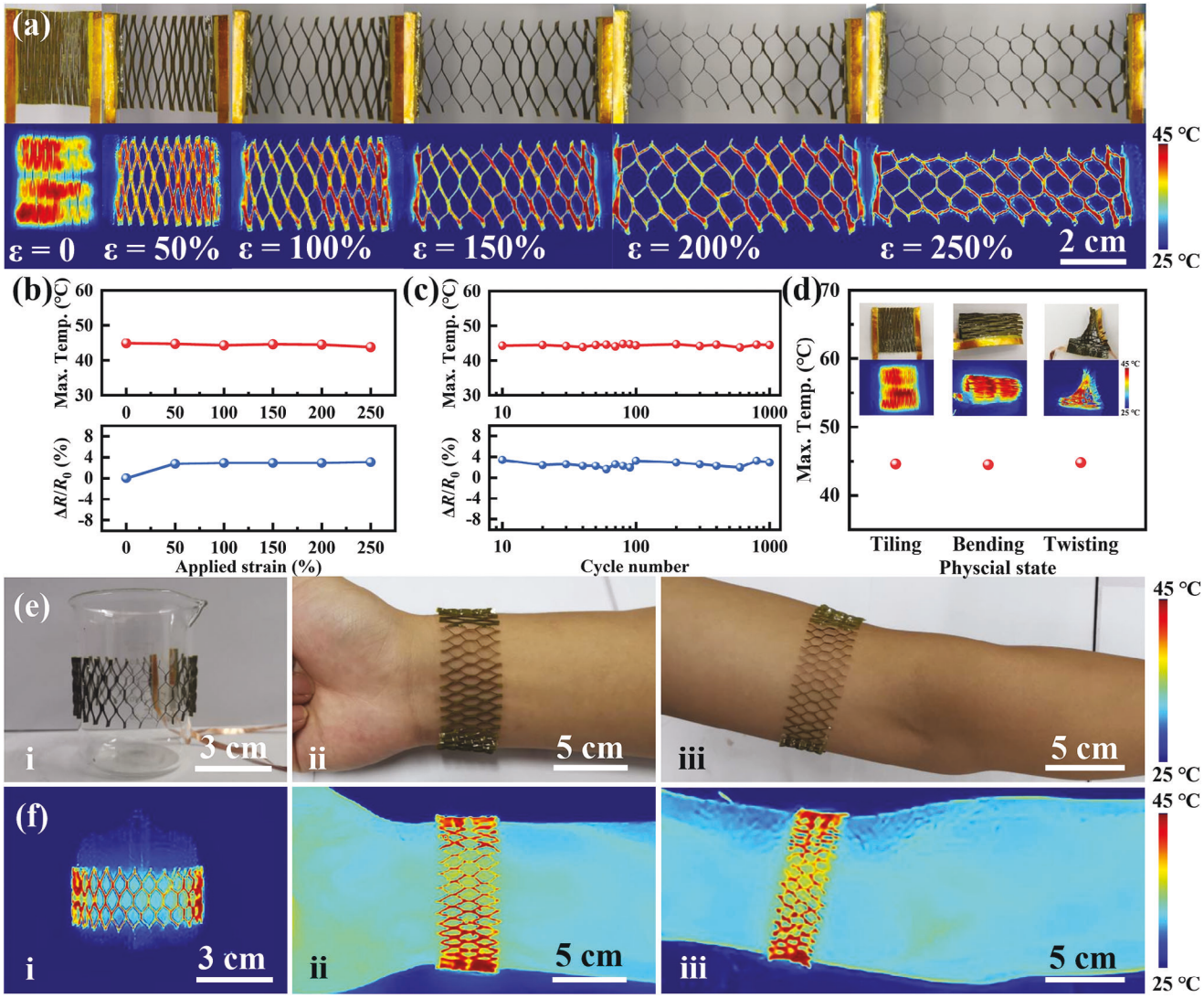

Figure 3. $Ti_3C_2T_x$-Ag@SNF composites-based kirigami-patterned stretchable heater. a) Optical and infrared thermal images of devices under various strains. Resistance change rate and maximum temperature of the heater operated at 2.5 V over b) increasing strain and c) 1000 cycles upon 250% stretching. d) Maximum temperature of the heater operated at 2.5 V upon tiling, bending, and twisting (with the corresponding optical and infrared thermal images shown in the inset). e) Optical and f) infrared images of the band-type heater attached to (i) a glass beaker, (ii) the wrist, and (iii) the arm.

electromagnetic waves from the composite into the air. Subsequently, the remaining incident electromagnetic waves penetrate into the multi-dimensional heterogeneous network of $Ti_3C_2T_x$-Ag@SNF and interact with a large number of free electrons to result in ohmic loss of the electromagnetic wave. In addition, the conductance mismatch at the heterogeneous interface between SNFs, AgNPs, and $Ti_3C_2T_x$ leads to charge accumulation and rearrangement at the interface to significantly enhance the polarization loss of electromagnetic energy.[49,50] Dipole polarization originating from the AgNPs/$Ti_3C_2T_x$ interface also converts the electromagnetic energy into thermal energy, further attenuating electromagnetic waves.[51–53] Finally, the multi-dimensional conductive network of $Ti_3C_2T_x$-Ag@SNF minimizes the escape of the incident electromagnetic waves, resulting in repeated attenuation and absorption of electromagnetic waves. In summary, the synergistic effect of varying electromagnetic wave attenuation mechanisms (i.e., surface reflection, ohmic loss, interface polarization, dipole polarization, and multiple reflections) provides $Ti_3C_2T_x$-Ag@SNF with exceptionally high EMI shielding efficiency of 50 dB.

The high-frequency electromagnetic waves from multiple sources can be effectively shielded by the $Ti_3C_2T_x$-Ag@SNF-based EMI shielding film For instance, turning on the Tesla coil can generate an induced voltage in the neon lamp array to light up the neon lamp, but the neon lamp goes out immediately after placing the $Ti_3C_2T_x$-Ag@SNF film between the Tesla coil and the neon lamp to shield the high-frequency electromagnetic wave (Figure 4e and Movie S1, Supporting Information). To mitigate the detrimental effects of electromagnetic waves on human health,[54] the EMI shielding bag based on

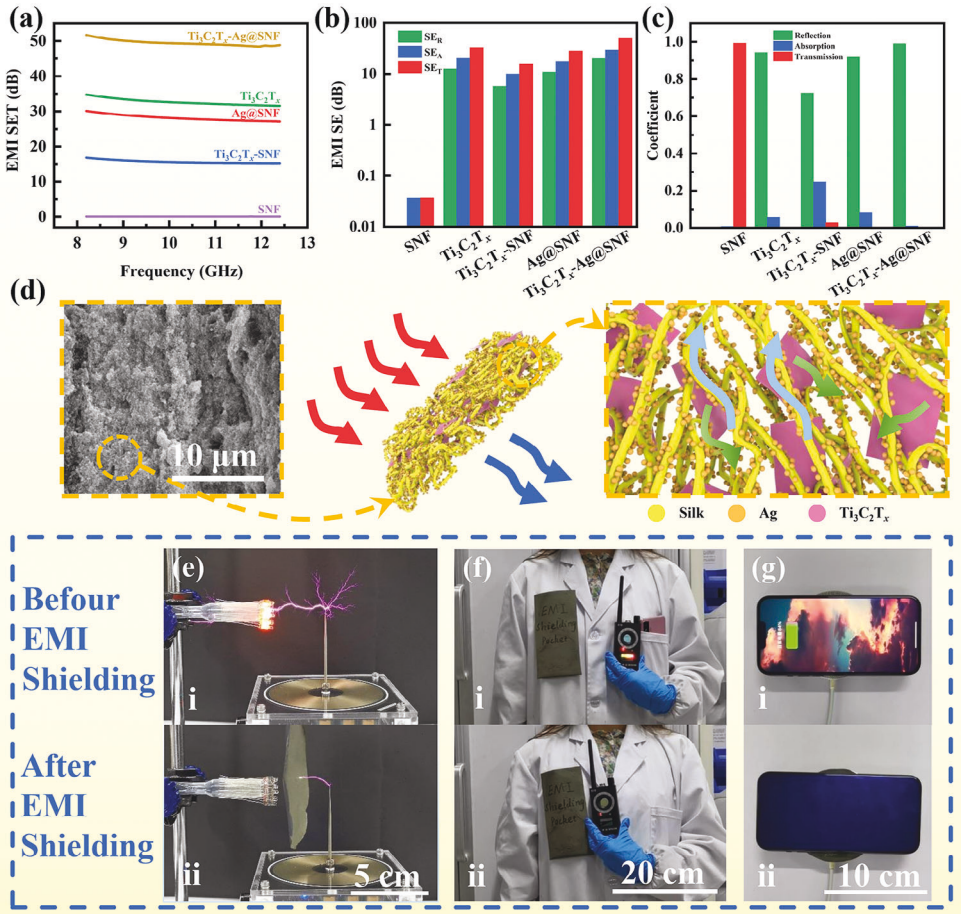

Figure 4. EMI shielding performance and applications of $Ti_3C_2T_x$-Ag@SNF composites. a) EMI shielding effectiveness, b) contributions and c) corresponding coefficients of reflection (SE_R), absorption (SE_A), and transmission (SE_T) from SNF, $Ti_3C_2T_x$, $Ti_3C_2T_x$-SNF composites, Ag@SNF composites, and $Ti_3C_2T_x$-Ag@SNF composites. d) SEM image of the cross-section and schematic illustration of the EMI shielding mechanism of $Ti_3C_2T_x$-Ag@SNF composites. Optical images of e) Tesla coil wireless power transmission, f) the signals received by the mobile phone, and g) the wireless charger charging the mobile phone in the (i) absence and (ii) presence of $Ti_3C_2T_x$-Ag@SNF composites.

$Ti_3C_2T_x$-Ag@SNF can significantly attenuate the signal from the smartphone placed inside (Figure 4f and Movie S2, Supporting Information). The $Ti_3C_2T_x$-Ag@SNF composite reinforced with polyethylene terephthalate (PET) film could also provide a large-scale EMI shielding film to even disrupt the wireless charging of the smartphone from the wireless charger when placed in between the two (Figure 4g and Movie S3, Supporting Information).

2.4. $Ti_3C_2T_x$-Ag@SNF Composites-Based TENG

The ultra-high electrical conductivity of $Ti_3C_2T_x$-Ag@SNF exhibits significant electron gain and loss capabilities when the composite comes into contact with different materials, indicating its use as a triboelectric layer in TENG. By using the negative $Ti_3C_2T_x$-Ag@SNF and positive Ecoflex-Ag as triboelectric film pairs, the basic working mechanism of TENG under the contact-separation mode is schematically illustrated (**Figure 5a**). Under a compressive force, the two triboelectric films will be brought into full contact, generating triboelectric charges distributed onto the surfaces of $Ti_3C_2T_x$-Ag@SNF and Ecoflex layers. By releasing the force, the two triboelectric films tend to separate from each other with an air gap, breaking the potential equilibrium between the two electrodes. The resulting potential difference drives the electrons to flow from $Ti_3C_2T_x$-Ag@SNF to Ag/Ecoflex via the load resistor, resulting in a positive instantaneous current. Conversely, the potential difference from the reduced distance between the two electrodes drives electrons to reflow from Ag/Ecoflex to $Ti_3C_2T_x$-Ag@SNF, generating a negative instantaneous current. Finally, the contact of the two triboelectric electrodes neutralizes all the generated charges. As a result, the periodic contact-separation process generates alternating currents through external loads. Moreover, the finite element method is used to analyze the potential distribution in the contact-separation process (Figure 5b). In the open-circuit state, there is no charge transfer and the potential difference is proportional to the distance between the two triboelectric films. It reaches the maximum value as the TENG returns to original state.

The characterizations of the electrical output performance of the $Ti_3C_2T_x$-Ag@SNF composites-based TENG include

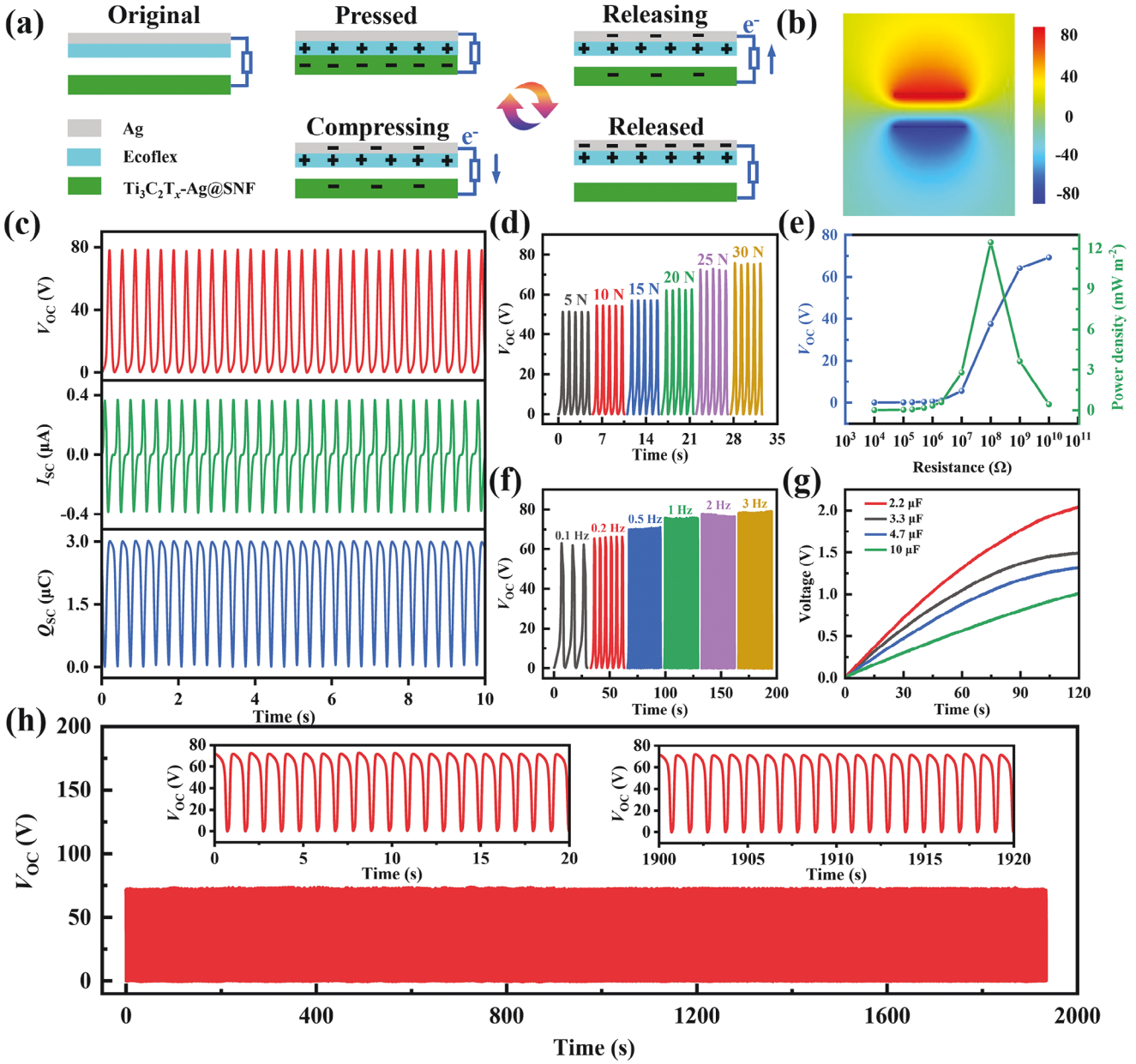

Figure 5. Performance characterizations of the $Ti_3C_2T_x$-Ag@SNF composites-based TENG. a) Schematic showing the working mechanism of $Ti_3C_2T_x$-Ag@SNF composites-based TENG. b) The potential difference between the two electrodes during the contact-separation process. c) The output voltage and current of the $Ti_3C_2T_x$-Ag@SNF composites-based TENG. The open-circuit voltages of $Ti_3C_2T_x$-Ag@SNF composites-based TENG under different loading d) pressures and e) frequencies. f) The output power density of the $Ti_3C_2T_x$-Ag@SNF composites-based TENG. g) Charging of the various capacitors with the $Ti_3C_2T_x$-Ag@SNF composites-based TENG. h) The stability test of the $Ti_3C_2T_x$-Ag@SNF composites-based TENG.

measurements of the open-circuit voltage (V_{OC}), short-circuit current (I_{SC}), and transfer charge (Q_{SC}). The maximum V_{OC}, I_{SC}, and Q_{SC} of $Ti_3C_2T_x$-Ag@SNF composites-based TENG are 78.37 V, 0.37 mA, and 2.99 μC, respectively, for a loading force of 30 N and frequency of 3 Hz (Figure 5c). It should be noted that the electrical output performance of $Ti_3C_2T_x$-Ag@SNF composites-based TENG closely depends on the loading force and frequency. For instance, the increase in the loading force on the $Ti_3C_2T_x$-Ag@SNF composites-based TENG (at 1 Hz) from 5 N to 30 N increases V_{OC} from 50 V to 75 V (Figure 5d), I_{SC} from 0.15 μA to 0.27 μA, and Q_{SC} from 1.94 μC to 2.82 μC (Figure S18, Supporting Information). Similarly, the increasing loading frequency from 0.1 Hz to 3 Hz increases the V_{OC} of the $Ti_3C_2T_x$-Ag@SNF composites-based TENG (at 30 N) from 62 V to 79 V (Figure 5e), I_{SC} from 0.05 μA to 0.37 μA, and Q_{SC} from 2.4 μC to 3 μC (Figure S19, Supporting Information).

While the output voltage increases from 0.01 V to 69.29 V as the resistance increases from 10^4 Ω to 10^{10} Ω, the output current decreases from 0.61 μA to 0.55 μA, resulting in the maximum power density of 12.46 mW m^{-2} at the resistance of 10^8 Ω

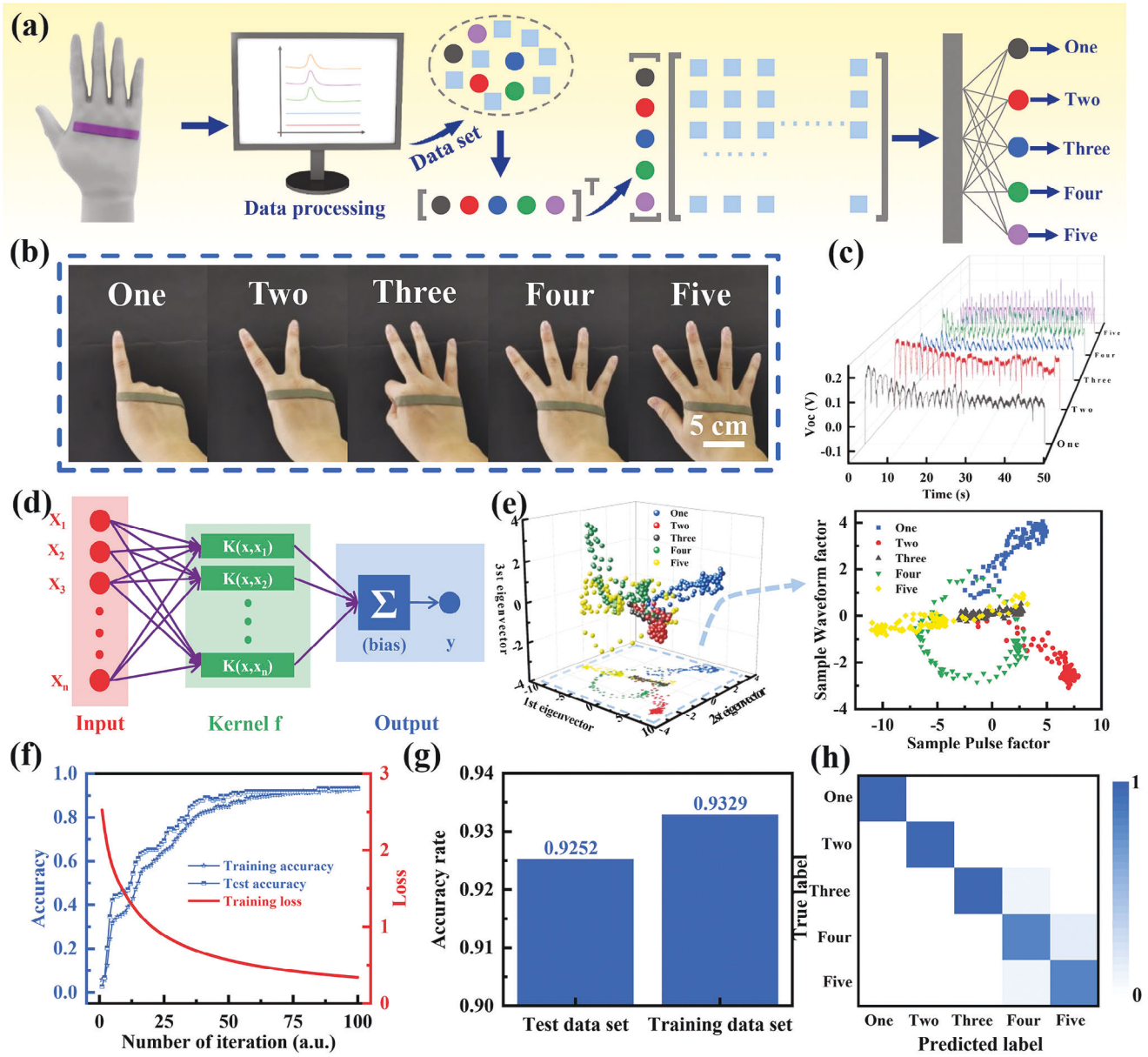

Figure 6. The self-powered intelligent detection system for human gestures. a) Schematic diagram showing the gesture data processing and classification/recognition based on the SVM algorithm. b) Optical images of the TENG on the hand with different gestures. c) Real-time voltage signals from different gestures. d) Typical structure of the SVM machine learning algorithm. e) A scatter plot containing the clustering results of 5 gestures and a sample plot of the dataset after PCA. f) Variation chart of loss and accuracy with the training cycle. g) Accuracy comparison between the training and test datasets. h) Confusion matrix to recognize five different gestures.

(Figure 5f). The generated power can rapidly charge commercial capacitors of varying capacitances (2.2, 3.3, 4.7, 10 μF) (Figure 5g). For instance, the capacitor of 2.2 μF can be charged to 2.04 V in 120 s for instantly lighting up 18 commercial LEDs connected in series (Figure S20 and Movie S4, Supporting Information). The $Ti_3C_2T_x$-Ag@SNF composites-based TENG also exhibits almost unchanged peak value and waveform in the output voltage over 1900 contact-separation cycles (Figure 5h), demonstrating high cycling stability.

The almost same voltage response of the $Ti_3C_2T_x$-Ag@SNF composite-based TENG to bending over the long and short axis direction both upward and downward indicates the negligibly small role of the bending direction (Figure S21, Supporting Information). When combined with the Support Vector Machine (SVM) classification algorithm (**Figure 6a**), the $Ti_3C_2T_x$-Ag@SNF composites-based TENG attached to the metacarpophalangeal joints on the back of the hand can recognize and classify human gestures with high accuracy even in the case of small sample datasets (Figure 6b,c; Figure S22, Supporting Information). After training the SVM algorithm with 30 cycles of five test gestures (Figure 6d), five gestures with clustered results in the scatter plot (Figure 6e) can be better separated in the sample plot

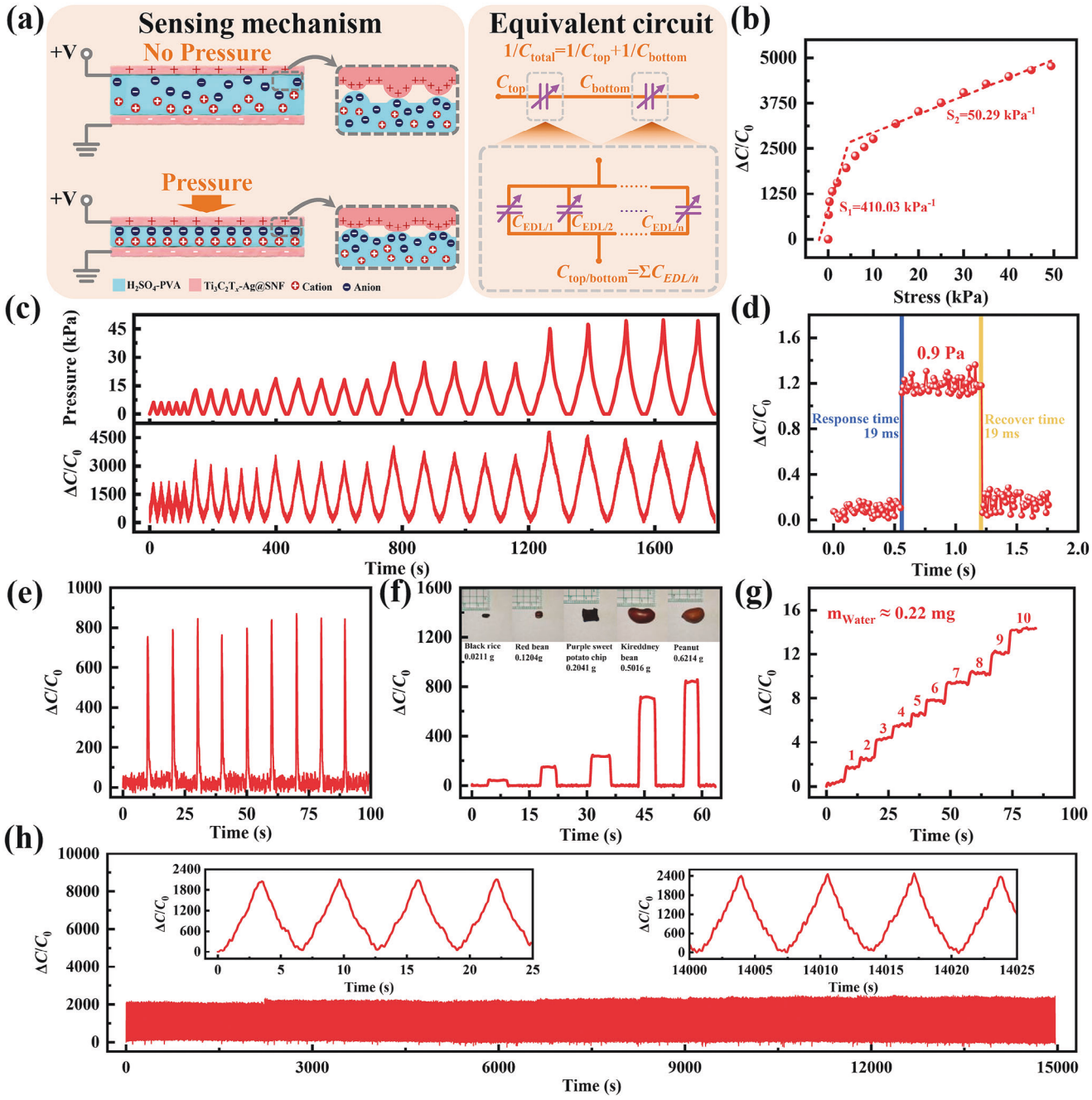

Figure 7. Pressure sensing performance of $Ti_3C_2T_x$-Ag@SNF composites-based pressure sensor. a) Schematic diagram of the sensing mechanism and b) sensitivity of $Ti_3C_2T_x$-Ag@SNF composites-based pressure sensor. c) Dynamic step test curves and d) response/recovery curves of $Ti_3C_2T_x$-Ag@SNF composites-based pressure sensor. Pressure sensor response to e) airflow, f) tiny objects with varying masses, and g) continuous water droplets. h) Stability of the pressure sensor.

after principal component analysis (PCA). However, it is still challenging to directly identify these five gestures. The algorithmic model achieves high classification accuracy in only 100 iterations, proving its feasibility and accuracy (Figure 6f). The resulting intelligent detection system exhibits a high accuracy of 92.52% in recognizing five different gestures in the testing set, which is slightly lower than 93.29% for the training set (Figure 6g,h).

2.5. $Ti_3C_2T_x$-Ag@SNF Composites-Based Pressure Sensor

Sandwiching the H_2SO_4-PVA ionic gel between two $Ti_3C_2T_x$-Ag@SNF films prepares a capacitive pressure sensor. As the electrons in $Ti_3C_2T_x$-Ag@SNF and the oppositely charged ions in H_2SO_4-PVA ionic gel accumulate at the contact interface to form an EDL with high capacitance, the resulting capacitive pressure sensor that can undergo microscopic deformations upon applied

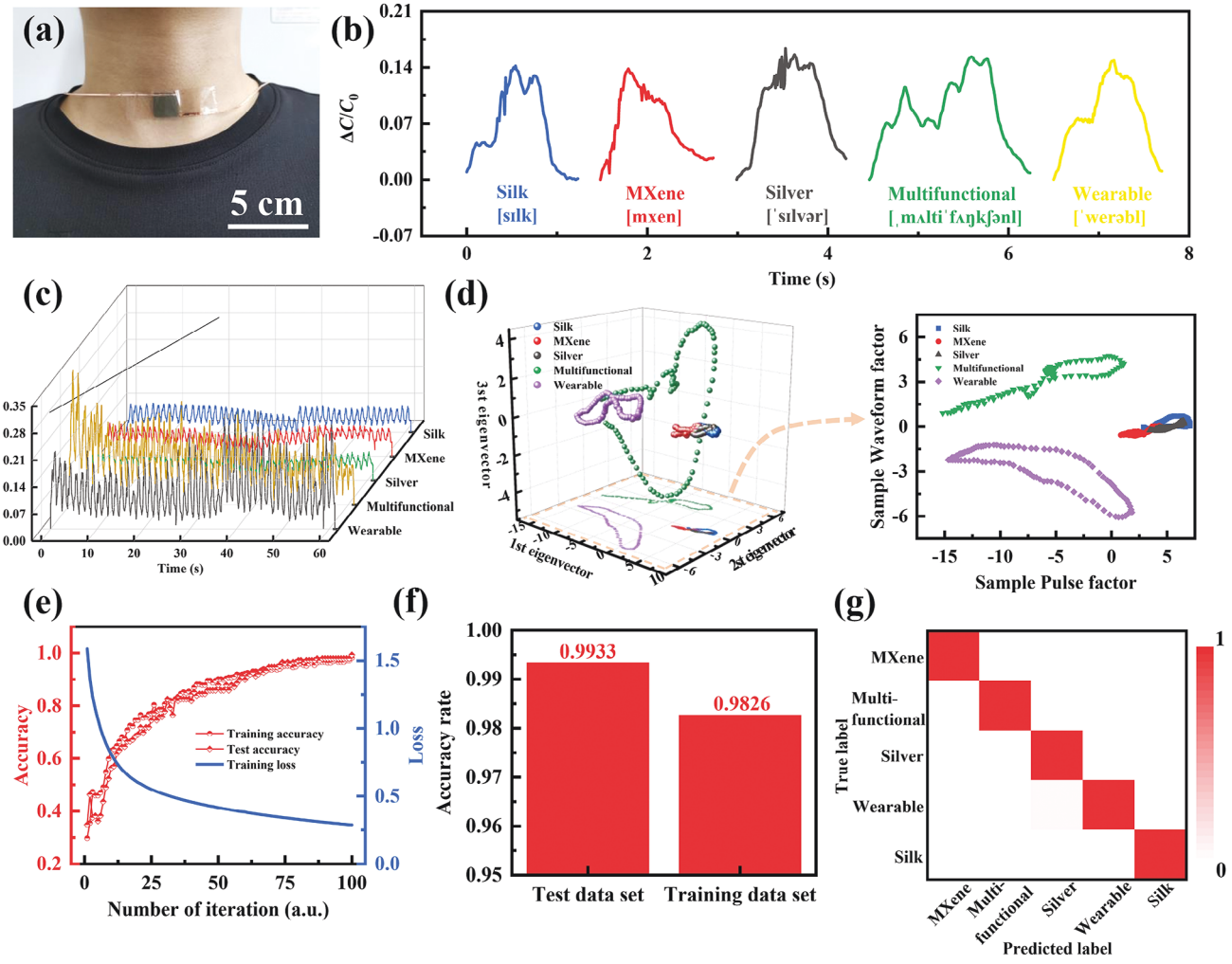

Figure 8. a) $Ti_3C_2T_x$-Ag@SNF composites-based pressure sensors are used in audible sound detection. b) Capacitance rate of change curves for different word pronunciations. c) Real-time capacitance rate-of-change signals from different word pronunciations. d) Scatterplot containing the clustering results for the pronunciation of 5 words, and a sample plot of the dataset after PCA. e) Variation chart of loss and accuracy with the training cycle. f) Accuracy comparison between the training and test datasets. g) Confusion matrix to recognize five different word pronunciations.

pressure exhibits significantly enhanced sensitivity (**Figure** 7a). Defined as the ratio of the capacitance change to pressure, the sensitivity is estimated as 410 kPa^{-1} in the pressure range from 0 to 6 kPa and 50 kPa^{-1} in the pressure range from 6 to 50 kPa (Figure 7b; Figure S23, Supporting Information). In Figure 7a, the equivalent circuit of the $Ti_3C_2T_x$-Ag@SNF composites-based pressure sensor is shown. The variable EDL capacitance (C_{EDL}) exists at both the contact interface of the H_2SO_4-PVA ionic gel the upper electrode (C_{top}) and the lower electrode (C_{bottom}). Thus, the total capacitance of the pressure sensor (C_{total}) is composed of two capacitors, C_{top} and C_{bottom}, in series. There is a relationship between $1/C_{total} = 1/C_{top}+1/C_{bottom}$. Therefore, the change of the contact area between $Ti_3C_2T_x$-Ag@SNF composites and H_2SO_4-PVA ionic gel is the direct cause of the significant change in the capacitance value of $Ti_3C_2T_x$-Ag@SNF composites-based pressure sensor. The mechanism is validated by the emergence of Warburg impedance (derived from the charge polarization process at the interface between $Ti_3C_2T_x$-Ag@SNF and H_2SO_4−PVA) as shown in the tailing line of the impedance pattern in the low-frequency region (Figure S24, Supporting Information). At the same time, the angle between the trailing line and the abscissa axis increases with the increasing applied pressure, which indicates the increase in the polarization capacitance of the two layers.

Besides a relatively stable and repeatable response to the same dynamic pressure over a relatively large range (Figure 7c), the pressure sensor also shows a fast response/recovery time of 19 ms to a small pressure of 0.9 Pa (Figure 7d). The rapid response/recovery and low detection limit allow the pressure sensor to detect the airflow generated by the ear wash ball (100 Pa) (Figure 7e), tiny objects with varying masses (Figure 7f; Figure S25, Supporting Information), and progressively added water droplets (1 Pa) (Figure 7g; Figure S26, Supporting Information). Together with excellent stability over 2400 cycles to 10 kPa (Figure 7h; Figure S27, Supporting Information), the demonstrated pressure sensor with excellent pressure sensing performances of high sensitivity over a wide sensing range, fast response/recovery, and low detection limit outperforms other

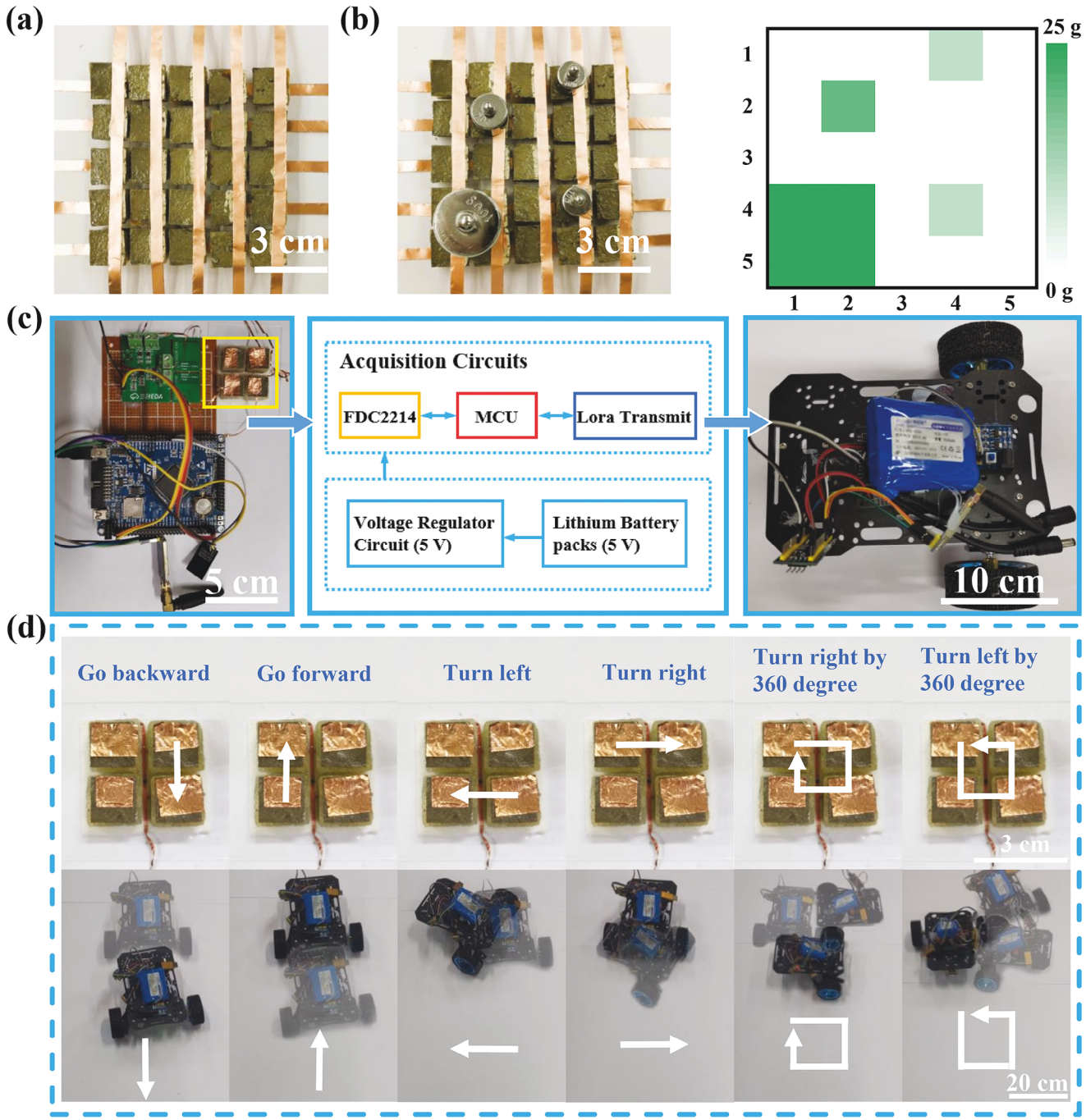

Figure 9. Applications of $Ti_3C_2T_x$-Ag@SNF composites-based pressure sensor as human-machine interface. a) Optical image of the 5 × 5 sensor array and b) the pressure distribution after placing four weights on top. c) Schematic diagram and d) demonstration of the human-machine interface with a 2 × 2 sensor array to control the trolley.

$Ti_3C_2T_x$- or Ag-based pressure sensors previously reported in the literature (Table S6, Supporting Information).

Monitoring the vocal cords is crucial for maintaining laryngeal health. Compared with the monitoring of joint motion, vocal cord vibration monitoring requires more sensitive sensors. $Ti_3C_2T_x$-Ag@SNF composites-based pressure sensors are affixed to the human throat area (**Figure** 8a), using the capacitance response curve to monitor the vibrations of the vocal cords as they pronounced the words "Silk", "MXene", "Silver", "Multifunctional", and "Wearable" (Figure 8b, c). Following PCA-based dimensionality reduction, the visual data demonstrates discernible distinctions among categories within the reduced-dimensional space, albeit with persistent overlap (Figure 8d). After 50 times of SVM algorithm training on the pronunciation of 5 words, the algorithm model can accurately classify the pronunciation after 100 iterations (Figure 8e). The recognition accuracy of the SVM-based

vocal recognition system for the five words in the test set is as high as 99.33%, which is slightly higher than 98.26% of the training set (Figure 8f,g).

Configuring the $Ti_3C_2T_x$-Ag@SNF composites-based pressure sensors into a 5 × 5 array (**Figure 9a**) can correctly capture the position and quality of the fruits with different weights on the array (Figure 9b). Combining a simple 2 × 2 sensor array with a lithium battery pack, a voltage regulation circuit, a wireless signal transmission unit, and a microprocessor results in an intelligent wireless human-machine interface to track the finger movement trajectory and wirelessly drive the trolley (Figure 9c). While the gestures of "↓"/"↑" move the trolley back/forward and the gestures of "←"/"→" turn the trolley to the left/right, the gesture "□" in the (counter)clockwise direction turns it around (Figure 9d and Movie S5, Supporting Information).

3. Conclusion

In summary, decorating the surface of 1D SNFs with conductive 0D AgNPs and 2D $Ti_3C_2T_x$ nanosheets forms multi-dimensional heterogeneous conductive $Ti_3C_2T_x$-Ag@SNF composites with ultrahigh conductivity of 142959 S m^{-1}. The kirigami-patterned $Ti_3C_2T_x$-Ag@SNF composites can provide the soft heaters with a high electrothermal conversion efficiency of 90% with a heating rate of 87 °C s^{-1} even upon stretching of 250%. The multi-dimensional heterogeneous conductive network of $Ti_3C_2T_x$-Ag@SNF composites also results in excellent EMI shielding performance with an EMI SE_T of 49.4 dB (10,088 dB cm^{-1}). Used as a triboelectric layer in the contact-separation mode, the $Ti_3C_2T_x$-Ag@SNF composites-based TENG exhibits a maximum V_{OC}, I_{SC}, and Q_{SC} of 78.37 V, 0.37 mA, and 2.99 μC, respectively. When combined with the SVM-based machine learning algorithm in a self-powered intelligent detection system, the single TENG-based sensor on the back of the hand can capture and recognize five human gestures with high accuracy (92.52%). Taken together with ionic gel, $Ti_3C_2T_x$-Ag@SNF composites can also provide capacitive pressure sensors with the EDL effect to feature a wide pressure sensing range (0–50 kPa), high sensitivity (410 kPa^{-1}), fast response/recovery time (19 ms), and low detection limit (0.9 Pa). The application of the pressure sensor (array) is showcased in human-machine interfaces to vocal cord sound monitoring and wirelessly control the movement of a trolley. The material design and proof-of-the-concept demonstrations of $Ti_3C_2T_x$-Ag@SNF composites in various device components highlight the future opportunity in all SNF-based wearable devices.

Supporting Information

Supporting Information is available from the Wiley Online Library or from the author.

Acknowledgements

N.Y. and C.Z. contributed equally to this work. This work was supported by the National Natural Science Foundation of China [Grant number 52103138, 52201043], the Natural Science Foundation of Fujian Province [Grant number 2023J01159], Starting Research Fund from Fujian University of Technology [GY-Z220199]. H.C. acknowledges the support from the National Institutes of Health (award No. R21EB030140), the National Science Foundation (grant Nos. 2309323, 2243979, 2319139, and 2222654), and Penn State University.

Conflict of Interest

The authors declare no conflict of interest.

Data Availability Statement

The data that support the findings of this study are available from the corresponding author upon reasonable request.

Keywords

human-machine interfaces, machine learning, silk nanofibers, Ti3C2Tx MXene, wearable electronics

Received: July 11, 2024
Revised: August 13, 2024
Published online: September 3, 2024

[1] Y. Ding, J. Jiang, Y. Wu, Y. Zhang, J. Zhou, Y. Zhang, Q. Huang, Z. Zheng, *Chem. Rev.* **2024**, *124*, 1535.
[2] S. Gong, Y. Lu, J. Yin, A. Levin, W. Cheng, *Chem. Rev.* **2024**, *124*, 455.
[3] M. Tan, Y. Xu, Z. Gao, T. Yuan, Q. Liu, R. Yang, B. Zhang, L. Peng, *Adv. Mater.* **2022**, *34*, 2108491.
[4] S. Zhao, J. Ahn, *Mater. Sci. Eng. R, Rep. : A Rev. J.* **2022**, *148*, 100672.
[5] Y. Niu, H. Liu, R. He, Z. Li, H. Ren, B. Gao, H. Guo, G. M. Genin, F. Xu, *Mater. Today* **2020**, *41*, 219.
[6] X. Wei, X. Liang, C. Meng, S. Cao, Q. Shi, J. Wu, *Soft Sci.* **2023**, *3*, 17.
[7] Y. Wang, R. Shu, X. Zhang, *Angew. Chem.-Int. Ed.* **2023**, *62*, 202303446.
[8] P. Nagwade, S. Parandeh, S. Lee, *Soft Sci.* **2023**, *3*, 24.
[9] X. Yang, X. Huang, X. Qiu, Q. Guo, X. Zhang, *Nat. Commun.* **2024**, *15*, 4553.
[10] Y. Liu, J. Ren, S. Ling, *Compos. Commun.* **2019**, *13*, 85.
[11] Z. A. Zianor Azrina, M. D. H. Beg, M. Y. Rosli, R. Ramli, N. Junadi, A. K. M. M. Alam, *Carbohydr. Polym.* **2017**, *162*, 115.
[12] E. H. Qua, P. R. Hornsby, H. S. S. Sharma, G. Lyons, *J. Mater. Sci.* **2011**, *46*, 6029.
[13] Y. Egi, A. Kontani, J. Kadokawa, *Int. J. Biol. Macromol.* **2023**, *253*, 127512.
[14] Z. Chen, Y. Hu, G. Shi, H. Zhuo, M. A. Ali, E. Jamróz, H. Zhang, L. Zhong, X. Peng, *Adv. Funct. Mater.* **2023**, *33*, 2214245.
[15] B. Hwang, A. Lund, Y. Tian, S. Darabi, C. Müller, *ACS Appl. Mater. Interfaces* **2020**, *12*, 27537.
[16] L. Ma, Q. Liu, R. Wu, Z. Meng, A. Patil, R. Yu, Y. Yang, S. Zhu, X. Fan, C. Hou, Y. Li, W. Qiu, L. Huang, J. Wang, N. Lin, Y. Wan, J. Hu, X. Y. Liu, *Small* **2020**, *16*, 2000203.
[17] C. Ye, J. Ren, Y. Wang, W. Zhang, C. Qian, J. Han, C. Zhang, K. Jin, M. J. Buehler, D. L. Kaplan, S. Ling, *Matter* **2019**, *1*, 1411.
[18] E. Steven, W. R. Saleh, V. Lebedev, S. F. A. Acquah, V. Laukhin, R. G. Alamo, J. S. Brooks, *Nat. Commun.* **2013**, *4*, 2435.
[19] R. Wu, L. Ma, C. Hou, Z. Meng, W. Guo, W. Yu, R. Yu, F. Hu, X. Y. Liu, *Small* **2019**, *15*, 1901558.
[20] M. Zhang, C. Wang, Q. Wang, M. Jian, Y. Zhang, *ACS Appl. Mater. Interfaces* **2016**, *8*, 20894.

[21] L. Zulan, L. Zhi, C. Lan, C. Sihao, W. Dayang, D. Fangyin, *Adv. Electron. Mater.* **2019**, *5*, 1800648.
[22] J. D. Ryan, D. A. Mengistie, R. Gabrielsson, A. Lund, C. Müller, *ACS Appl. Mater. Interfaces* **2017**, *9*, 9045.
[23] S. Ling, Q. Wang, D. Zhang, Y. Zhang, X. Mu, D. L. Kaplan, M. J. Buehler, *Adv. Funct. Mater.* **2018**, *28*, 1705291.
[24] Z. Lu, C. Mao, H. Zhang, *J. Mater. Chem. C.* **2015**, *3*, 4265.
[25] C. Wang, K. Xia, M. Jian, H. Wang, M. Zhang, Y. Zhang, *J. Mater. Chem. C.* **2017**, *5*, 7604.
[26] W. He, C. Wang, H. Wang, M. Jian, W. Lu, X. Liang, X. Zhang, F. Yang, Y. Zhang, *Sci. Adv.* **2019**, *5*, eaax649.
[27] C. Wang, X. Li, E. Gao, M. Jian, K. Xia, Q. Wang, Z. Xu, T. Ren, Y. Zhang, *Adv. Mater.* **2016**, *28*, 6640.
[28] C. Liu, Z. Feng, T. Yin, T. Wan, P. Guan, M. Li, L. Hu, C. H. Lin, Z. Han, H. Xu, W. Chen, T. Wu, G. Liu, Y. Zhou, S. Peng, C. Wang, D. Chu, *Adv. Mater.* **2024**, https://doi.org/10.1002/adma.202403791.
[29] L. Liu, J. Feng, Y. Xue, V. Chevali, Y. Zhang, Y. Shi, L. C. Tang, P. Song, *Adv. Funct. Mater.* **2023**, *33*, 2212124.
[30] P. He, Z. Liu, G. Mao, Q. Liu, M. Zheng, R. Zuo, W. Cao, Z. Hou, J. Yuan, M. Cao, *Composites, Part A* **2022**, *157*, 106935.
[31] R. Qin, J. Nong, K. Wang, Y. Liu, S. Zhou, M. Hu, H. Zhao, G. Shan, *Adv. Mater.* **2024**, *36*, 2312761.
[32] D. Wang, L. Wang, Z. Lou, Y. Zheng, K. Wang, L. Zhao, W. Han, K. Jiang, G. Shen, *Nano Energy* **2020**, *78*, 105252.
[33] L. X. Liu, W. Chen, H. B. Zhang, Q. W. Wang, F. Guan, Z. Z. Yu, *Adv. Funct. Mater.* **2019**, *29*, 1905197.
[34] Q. Huang, Y. Yang, R. Chen, X. Wang, *Ecomat* **2021**, *3*, e12076.
[35] Z. Xie, L. Yao, H. Fang, Z. Yang, X. Zhou, L. Lin, J. Xie, Y. Zhang, *Small* **2024**, *20*, 2310191.
[36] S. Yan, Q. Wang, Z. Tariq, R. You, X. Li, M. Li, Q. Zhang, *Int. J. Biol. Macromol.* **2018**, *118*, 775.
[37] Y. Chen, C. Rong, W. Gao, S. Luo, Y. Guo, Y. Gu, G. Yang, W. Xu, C. Zhu, L. Qu, *J. Colloid Interface Sci.* **2024**, *653*, 540.
[38] W. Eom, H. Shin, T. H. Han, *Appl. Phys. Lett.* **2023**, *122*, 211601.
[39] M. Peng, L. Wang, L. Li, X. Tang, B. Huang, T. Hu, K. Yuan, Y. Chen, *Adv. Funct. Mater.* **2022**, *32*, 2109524.
[40] A. M. Abdel-Mohsen, J. Jancar, L. Kalina, A. F. Hassan, *Carbohydr. Polym.* **2020**, *234*, 115861.
[41] D. W. Boukhvalov, I. S. Zhidkov, E. Z. Kurmaev, E. Fazio, S. O. Cholakh, L. D'Urso, *Carbon* **2018**, *128*, 296.
[42] S. Yan, Q. Yang, G. Han, Q. Wang, X. Li, L. Wang, Z. Luo, R. You, Q. Zhang, *New J. Chem.* **2019**, *43*, 2559.
[43] Y. Luo, Y. Xie, W. Geng, J. Chu, H. Wu, D. Xie, X. Sheng, Y. Mei, *J. Mater. Sci. Technol.* **2022**, *129*, 27.
[44] M. Weng, J. Zhou, Y. Ye, H. Qiu, P. Zhou, Z. Luo, Q. Guo, *J. Colloid Interface Sci.* **2023**, *647*, 277.
[45] Z. Fan, L. Lu, M. Sang, J. Wu, X. Wang, F. Xu, X. Gong, T. Luo, K. C. F. Leung, S. Xuan, *Adv. Sci.* **2023**, *10*, 2302412.
[46] X. Li, M. Yang, W. Qin, C. Gu, L. Feng, Z. Tian, H. Qiao, J. Chen, J. Chen, S. Yin, *Colloids Surf. A* **2023**, *658*, 130706.
[47] Q. Song, F. Ye, X. Yin, W. Li, H. Li, Y. Liu, K. Li, K. Xie, X. Li, Q. Fu, L. Cheng, L. Zhang, B. Wei, *Adv. Mater.* **2017**, *29*, 1701583.
[48] M. Zhang, C. Han, W. Cao, M. Cao, H. Yang, J. Yuan, *Nano-Micro Lett.* **2020**, *13*, 27.
[49] M. Sun, W. Cao, P. Zhu, Z. Xiong, C. Chen, J. Shu, W. Huang, F. Wu, *Adv. Compos. Hybrid Mater.* **2023**, *6*, 54.
[50] J. Liu, M. Yu, Z. Yu, V. Nicolosi, *Mater. Today* **2023**, *66*, 245.
[51] Y. Zhang, M. Xu, Z. Wang, T. Zhao, L. Liu, H. Zhang, Z. Yu, *Nano Res.* **2022**, *15*, 4916.
[52] L. Wang, Z. Ma, H. Qiu, Y. Zhang, Z. Yu, J. Gu, *Nano-Micro Lett.* **2022**, *14*, 224.
[53] W. Huang, X. Zhang, J. Chen, Q. Qiu, Y. Kang, K. Pei, S. Zuo, J. Zhang, R. Che, *Adv. Sci.* **2023**, *10*, 2303217.
[54] N. Wang, W. Zou, X. Li, Y. Liang, P. Wang, *RSC Adv.* **2022**, *12*, 17158.